Nature Communications

https://doi.org/10.1038/s41467-026-73659-z

Article in Press

Monolithically integrated photon-mapping infrared imager

Received: 11 November 2025

Accepted: 18 May 2026

Cite this article as: Han, X., Wang, J., Guo, L. *et al.* Monolithically integrated photon-mapping infrared imager. *Nat Commun* (2026). https://doi.org/10.1038/s41467-026-73659-z

Xingwei Han 韩兴伟, Jun Wang 王军, Lei Guo 郭磊, Shikun Duan 段世坤, Jiayue Han 韩嘉悦, Meiyu He 何美誉, Chao Han 韩超, He Yu 于贺, Jun Gou 苟君 & Weida Hu 胡伟达

Monolithically Integrated Photon-Mapping Infrared Imager

Xingwei Han (韩兴伟)[1,2†], Jun Wang (王军)[1†*], Lei Guo (郭磊)[1†], Shikun Duan (段世坤)[3†], Jiayue Han (韩嘉悦)[1], Meiyu He (何美誉)[1], Chao Han (韩超)[1], He Yu (于贺)[1], Jun Gou (苟君)[1], Weida Hu (胡伟达)[3*]

1. State Key Laboratory of Electronic Thin Films and Integrated Devices, University of Electronic Science and Technology of China, Chengdu 610054, China
2. Southwest Institute of Technical Physics, Chengdu 610041, China
3. State Key Laboratory of Infrared Physics, Shanghai Institute of Technical Physics, Chinese Academy of Sciences, Shanghai 200083, China

†These authors contributed equally to this work.
*Corresponding author E-mail: wjun@uestc.edu.cn; wdhu@mail.sitp.ac.cn

Abstract

Conventional infrared imaging systems rely heavily on external power supplies, limiting their applicability, flexibility, and portability. Here, we present a monolithically integrated photon-mapping near-infrared (780-900 nm) imager that operates in a self-driven mode, achieving a resolution of 5799 ppi and a frame rate of 18.5 kHz. The device vertically integrates multiple photovoltage-generating light-sensing units with a light-emitting unit in a cascaded configuration, enabling visible emission upon near-infrared excitation via internal carrier transfer. Its circuit-free architecture confers intrinsic flexibility and large-area scalability while remaining fully compatible with room-temperature operation. The system eliminates the need for pixel-level readout, thereby enabling spatial resolution beyond conventional pixel limits under optical excitation control. It further supports high-speed imaging governed by the transit dynamics of photogenerated carriers. In addition, its self-driven characteristic ensures inherently low background noise, enhancing the signal-to-background ratio and improving imaging quality. This work introduces a simplified, energy-efficient approach to infrared visualization.

Introduction

Infrared imaging technology captures images by detecting an object's inherent or reflected infrared radiation. Unlike conventional visible-light imaging systems, infrared imaging can operate under low human-visible light or even in complete darkness, making it an invaluable tool for numerous applications[1-3]. Over the past few decades, this technology has gained significant importance across various sectors due to its unique ability to provide visual information in situations where visible light is insufficient or unavailable. Its extensive use in critical fields, such as military surveillance, security systems, medical diagnostics, and industrial monitoring, is well documented[4-7]. Consequently, infrared imaging technology is gradually becoming a foundational component of modern electronic systems, with growing integration into both consumer and professional applications[8-11].

Conventional infrared imaging systems typically comprise sensitive detection arrays, readout integrated circuits (ROICs), image processing systems, and optical displays[12,13]. These imaging systems utilize a range of detection technologies, including photon-based infrared detectors (e.g., silicon (Si)[14], cadmium mercury telluride (HgCdTe)[15], indium gallium arsenide (InGaAs)[16], lead sulfide (PbS)[17,18], and quantum well structures[19]) and thermoelectric-based detectors (e.g., vanadium oxide (VO_x)[20], pyroelectric materials[21], and thermocouple materials[22]). Irrespective of the detection mechanism, such systems rely on ROICs to convert the infrared signals captured by the detection array from optical to electrical form. The image-processing and display circuits subsequently process the electrical signals, converting them into optical signals and ultimately producing visible light output (Fig. 1a). Fabricating ROICs and associated image-processing systems requires advanced semiconductor manufacturing techniques. These high-precision processes not only increase overall production costs but also impose significant limitations on scalability, portability, lightweight design, and the widespread application of infrared imaging technology[23,24]. Moreover, conventional focal plane array (FPA) infrared imaging is limited by pixel size and ROIC readout speed, with both spatial resolution and frame rate approaching their fundamental limits.

To address these challenges, researchers have proposed upconversion devices comprising an infrared detection unit coupled with a light-emitting diode. These devices enable the direct conversion of low-frequency infrared light into higher-frequency visible light, eliminating the need for complex readout and processing circuits and thereby allowing direct visualization of infrared

signals[25-27]. Stacking multiple light-emitting units (LEUs) in series can significantly enhance the photon-to-photon conversion efficiency ($\eta_{p\text{-}p}$) of such devices, thereby alleviating the issue of low efficiency (Supplementary Table 1)[28,29]. However, the operation of upconversion devices still relies on the photogenerated potential produced in the light-sensing unit (LSU) to drive the LEU, which is typically insufficient for independent operation. As a result, existing upconversion imaging devices still require external circuitry and power supplies[30,31]. This dependence restricts their applicability, flexibility, and portability, while eliminating it would pave the way for broader and more practical applications[32-34]. *Ding et al.* developed a self-driven microscale optoelectronic upconversion device based on inorganic materials[35]. However, the relatively large lateral carrier diffusion in the inorganic stacked structure necessitates pixelated arrays for infrared imaging and makes flexible implementation challenging.

In this study, we propose a monolithically integrated photon-mapping near-infrared (780-900 nm) imaging technology that requires neither pixelated arrays nor external power supply, while offering large-area capability, flexibility, low background (BG) noise, high resolution, and high frame rates (Fig. 1b). Unlike FPA-based approaches, photon-mapping infrared imager (PMII) avoids the resolution bottleneck imposed by pixel size and the speed limitation of ROIC readout circuits, achieving 5799 ppi resolution and a 18.5 kHz frame rate. In contrast to upconversion devices, PMII eliminates the reliance on external circuitry and power supplies, thereby reducing power consumption and enabling fully flexible, lightweight (15.58 mg) devices capable of infrared imaging in a self-driven mode. The cascaded photovoltaic response enables this characteristic by generating a open-circuit voltage (V_{oc}) that exceeds the V_{on} of the LEU, thereby directly driving light emission without an external bias. The PMII employs a monolithically integrated device architecture comprising 28 vertically stacked functional thin films, including five serially connected LSUs and one LEU, and attains substantially lower imaging thresholds and enhanced clarity in comparison to commercial infrared viewing cards. Furthermore, PMII enables high-quality infrared imaging of fine biological structures. This innovative approach not only advances monolithic optoelectronic integration but also reduces system complexity and cost, providing a pathway for the broad application of infrared imaging technologies.

Results

Device design

In regions without infrared illumination, the charge generation layer (CGL) remains unexcited, generating neither photocarriers nor photovoltage, and the LEU stays in a stable dark state. Conversely, under infrared irradiation, the LSUs absorb the incident photons, and the photopotentials generated by each CGL cumulatively build up through the serial configuration. Once the accumulated photopotential exceeds the V_{on} of the LEU, visible emission is triggered (Fig. 1c). This entire process operates without the need for external power sources or additional circuit control, thus realizing a truly self-driven imaging capability. Such a mechanism is particularly advantageous in scenarios where conventional power supplies are limited or unavailable. Additionally, the self-driven mechanism inherently exhibits low BG noise, thereby significantly enhancing the signal-to-background ratio (SBR) and improving infrared imaging quality (Supplementary Figs. 1 and 2).

To achieve the self-driven effect of PMII, multiple inverted LSUs were deposited beneath the green phosphorescent LEU, with the LSUs interconnected via an intermediate connection layer (ICL) (Supplementary Fig. 3). For the proposed PMII, the bottom ITO and top metal electrodes are directly connected, enabling direct infrared visualization upon infrared excitation. The energy-dispersive X-ray spectroscopy elemental distribution and transmission electron microscopy images of the interfaces reveal well-defined, smooth layered structures (Fig. 1d and Supplementary Fig. 4). The PMII consists of five stacked LSUs and an LEU. Four ICL layers interconnect the five-layer CGL to form series-connected LSUs, which are subsequently integrated with the LEU through thermal evaporation. The CGL employs a bulk heterojunction of the polymer D18-Cl and the non-fullerene acceptor L8-BO. This light-absorbing system enables high V_{oc} in organic detectors[36,37]. The ICL is composed of MoO_3/Ag/ZnO nanoparticles/PEIE. The LEU consists of TAPC/CBP: 7%$Ir(ppy)_2(acac)$/B_3PyMPM/LiF/Al. The molecular structures of these materials are shown in Supplementary Fig. 5. After the deposition of multiple layers, the atomic force microscopy measurements indicate that the film maintains a low roughness of 1.29 nm, ensuring effective interlayer connections and efficient carrier transport in the multilayer device (Supplementary Fig. 6). The proposed PMII enables real-time infrared visualization and imaging without auxiliary components (Supplementary Fig. 7). It further offers large-area, flexibility, low BG noise, high resolution, and high frame rate, enabling nondestructive detection of biological structures (Fig. 1e, Supplementary Figs. 8 and 9). With an sub-micron design (~800 nm), a 1.5 × 1.5 cm^2 PMII weighs only ~15.58 mg, underscoring its lightweight nature (Supplementary Fig.

10). In addition, the PMII shows superior performance in power consumption, structural flexibility, room-temperature operation, refresh rate, and cost-effectiveness, positioning it as an ideal candidate for next-generation portable, wearable, and monolithically integrated infrared visualization systems (Supplementary Fig. 11).

Device performance

The CGL exhibits strong absorption in the near-infrared region, while the LEU emits green light peaking at 523 nm (Fig. 2a). Owing to the high V_{oc} of the absorption system, along with the low V_{on} and high external quantum efficiency of the LEU (Fig. 2b and Supplementary Fig. 12), the device demonstrates self-driven light emission (Fig. 2c). The PMII exhibits no visible emission without infrared illumination; upon infrared excitation, self-driven emission emerges, yielding visible light that replicates the laser spot profile.

Distinct from conventional infrared imagers, this study focuses on the performance of the PMII in self-driven mode. When the input light power exceeds 80 μW cm^{-2}, the device begins self-driven emission (defined as 'turned on' when the luminance exceeds 0.1 cd m^{-2}, Supplementary Text 1), and maintains consistent luminance across various bias voltages (Fig. 2d). At an input light power of 280 mW cm^{-2}, the maximum luminance in self-driven mode reaches 47.2 cd m^{-2}, which is fundamental for achieving self-driven imaging. Under applied bias, the maximum luminance increases to 362.3 cd m^{-2}. Additionally, the emission spectra under different incident light powers show that the peak wavelength remains at 523 nm in the self-driven mode, with the full width at half maximum remaining at 48 nm (Fig. 2e), consistent with that of a standalone LEU. This spectral stability is advantageous for the accuracy of device performance characterization.

The device maintains linearity within the range of 200 μW cm^{-2} to 8 mW cm^{-2}, with a luminance linear dynamic range (*L*-LDR) of 33 dB (Fig. 2f). The inset shows that the *L*-LDR increases with applied bias, reaching 68 dB at 8 V. Additionally, the variation of current density exhibits a similar linear dynamic range, with a 36 dB range in self-driven mode (Fig. 2g). The current exhibits greater linearity than the luminance due to the repeated absorption of visible light by LSUs at low intensity. Similarly, for devices with four and three stacked LSUs, higher luminance and larger *L*-LDR were observed under bias conditions (Supplementary Fig. 13). This is due to the reduced thickness of the device's CGL resulting from fewer stacked LSUs, which reduces reabsorption of emitted light. Consequently, the luminance is higher at low input light

power for devices with four and three stacked LSUs, and the *L*-LDR increases accordingly. However, in self-driven mode, the luminance gradually deviates from linearity as the number of stacked LSUs decreases, eventually resulting in no light emission. This is primarily due to the lower photogenerated potential produced by an insufficient number of stacked LSUs, which is inadequate to effectively drive the LEU, thus posing challenges for effective imaging. To address this, we employed five stacked LSUs, ensuring that the PMII maintains sufficiently high luminance linearity for imaging applications.

The $\eta_{p\text{-}p}$ is the ratio of emitted visible light photons to incident infrared photons, where $\eta_{p\text{-}e}$ represents the ratio of photogenerated electrons to absorbed infrared photons, and $\eta_{e\text{-}p}$ is the ratio of emitted visible light photons to injected electrons[38]. The relationship between device efficiency and incident light power in self-driven mode is shown in Fig. 2h. As the incident light power increases, the absorption of LSU gradually saturates, leading to a decrease in $\eta_{p\text{-}e}$. In contrast, the $\eta_{e\text{-}p}$ remains relatively steady at low light power, as the photogenerated carriers of the LSU are insufficient to fully saturate the LEU. As luminance increases, the LEU's emission efficiency decreases, a trend consistent with that observed in the standalone LEU (Supplementary Fig. 12b). These factors collectively cause $\eta_{p\text{-}p}$ to decrease gradually, reaching a maximum of 0.116% at an incident light power of 270 μW cm^{-2}. As the bias voltage increases, the device's $\eta_{p\text{-}p}$ gradually approaches saturation, reaching a maximum of 0.171% at 8 V (Supplementary Fig. 14). The relatively low $\eta_{p\text{-}p}$ is mainly attributed to enhanced recombination of photogenerated carriers in the series-connected LSUs (Supplementary Fig. 15 and Supplementary Table 2). Moreover, an excessively thick or thin CGL would further reduce $\eta_{p\text{-}p}$ (Supplementary Fig. 16).

To further demonstrate the advancement of this work, we compared PMII with state-of-the-art infrared imaging techniques with respect to resolution and operating voltage (Fig. 2i, Supplementary Tables 3 and 4). The PMII differs fundamentally from these infrared imaging devices, as it converts infrared photons to visible photons solely in an optically controlled self-driven mode, without external electrical control, while offering higher resolution. The mechanism for achieving high resolution in self-driven mode arises from the transport behaviour of photogenerated carriers (Supplementary Fig. 17). During transfer between LSU and LEU, carriers inevitably undergo lateral diffusion within the hole transport layer. Under applied bias, an electric field exists throughout the entire device, allowing laterally diffused carriers to contribute to emission. In contrast, in self-driven mode, the photogenerated electric field is confined to the

illuminated region, preventing laterally diffused carriers from contributing to emission and thereby enabling higher spatial resolution.

Analysis of the internal mechanism

To analyze the operating mechanism of PMII, the individual LSUs and the LEU were investigated. Analysis of the current density-voltage characteristics reveals that as the number of stacked LSUs increases, the V_{oc} of the LSU also increases gradually (Fig. 3a). When the number of stacked layers reaches three, the V_{oc} of the LSUs surpasses the V_{on} of the LEU, and with five stacked layers, the current density tends to stabilize. This stabilization indicates that the sufficiently high V_{oc} of the LSUs, which effectively activate the LEU, enables stable and high-performance light emission and imaging. Different V_{oc} values of the LSUs are obtained by varying the input infrared light power (Fig. 3b). For a device with five stacked LSU layers, the V_{oc} exceeds the V_{on} of the LEU at an input power of 80 μW cm^{-2}, whereas for the device with three stacked LSU layers, the V_{oc} only reaches this level at 18 mW cm^{-2}. This result is consistent with the luminance performance shown in Supplementary Fig. 13. The statistical data obtained from eight devices present sufficient reliability, validating the stability of the results (Fig. 3c). The stability of the V_{oc} generated by LSUs with different stacking numbers also ensures the luminance stability of the PMII. Therefore, the decrease in luminance stability for the PMII with three stacked LSUs originates from the lower V_{oc}, which results in reduced luminance.

To investigate the driving effect of the LSUs on the LEU, we directly connected a five-layer stacked LSU in series with the LEU, without applying any external bias. Infrared light was incident on the LSU, and the LEU's light emission was simultaneously measured. In self-driven mode, the device maintains an *L*-LDR of 47 dB, which is higher than that of the PMII (Fig. 3d). This is because the visible light emitted by the LEU is not reabsorbed by the LSU, resulting in significantly higher luminance compared to the PMII (Supplementary Table 5). The luminance remains linear in the range of 0.48 to 131.9 cd m^{-2}, and the device maintains linearity even at a low incident light power of 80 μW cm^{-2}, whereas the PMII does not maintain linearity due to reabsorption. However, because the photogenerated carriers produced by the LSUs are randomly distributed across the entire LEU plane, this device with an external circuit connection is unsuitable for pixel-less infrared imaging. These observations indicate that the effective imaging capability

of our PMII primarily arises from the driving effect of the LSUs on the LEU under the photovoltaic effect, as well as the vertical stacking architecture.

The f_{-3dB} of the PMII is 10 kHz, indicating that it can operate under high-frequency modulation conditions (Fig. 3e). Conventional imaging systems are limited by complex scanning processes of pixelated detector arrays and electrical signal processing, resulting in relatively low imaging RFR, typically below 1 kHz (Supplementary Table 4). In comparison, our PMII exhibits a rise time of 29.5 μs and a fall time of 24.5 μs, with t_r defined as 10%-90% and t_f as 90%-10% (Fig. 3f and Supplementary Fig. 18). Benefiting from its fast response, the refresh rate (RFR)[39], calculated as $RFR = \frac{1}{t_r + t_f}$, reaches approximately 18.5 kHz.

In the zero-bias (self-driven) mode, the PMII maintains a lower background current and a higher SBR, representing a key advantage over conventional infrared imagers that rely on external bias (Fig. 3g). As the bias increases, the noise spectral density rises significantly (Fig. 3h). Imaging tests further confirm that the PMII produces clear emission images in the self-driven mode, whereas pronounced BG noise emerges under high-bias operation (Fig. 3i).

Applications

Most commercial near-infrared viewing cards rely on upconversion fluorescent materials, phosphorescent materials, and other special materials, which are laminated and encapsulated to enhance mechanical strength for infrared visualization. However, these infrared-viewing cards are limited by the materials' sensitivity, resulting in poor response to weak infrared signals, a narrow dynamic range, and difficulty distinguishing light signals below 1 mW cm^{-2}. This work compares the actual light emission performance of the PMII with that of commercial infrared-viewing cards under varying incident light powers (Fig. 4a and Supplementary Movie 1). When illuminated with a circular light spot, our PMII distinctly reproduces its true outline with superior infrared display capability, whereas the infrared-viewing card shows scattered emission with uneven luminance, obscuring the actual spot boundary. The PMII not only features self-emission without an external power supply, similar to commercial infrared-viewing cards, but also offers high sensitivity and effective imaging capabilities.

Moreover, conventional imagers rely on rigid electronic components, preventing them from operating correctly under bending conditions. In contrast, our PMII leverages the flexibility of

organic materials, enabling fully flexible operation. We explored the use of a PET flexible substrate to replace the glass substrate, enabling self-driven infrared visualization under flexible fabrication and bending conditions (Fig. 4b and Supplementary Movie 2). After 500 bending cycles with a bending radius of 5 mm, the luminance of the flexible device remained stable, with the peak luminance only decreasing from 46 to 36 cd m^{-2}, still sufficient for infrared visualization. These results indicate that the flexible device exhibits good robustness. Moreover, its compatibility with large-area fabrication makes it promising for practical applications (Supplementary Movie 3, under 850 nm illumination).

To evaluate the spatial resolution of the PMII, a dedicated test setup was constructed (Supplementary Fig. 19). The device clearly resolves alternating light and dark stripes with a minimum spacing of 4.38 μm, corresponding to a resolution of 5799 ppi (Fig. 4c). In this architecture, the resolution is primarily determined by the optical projection conditions and the lateral carrier diffusion within the device rather than the lithographically defined pixel size. Consistent with theoretical analysis, the single-LSU device exhibits reduced contrast and resolution under high bias (Supplementary Fig. 20). This high spatial resolution, combined with the superior penetration of the near-infrared band compared to visible light, enables the PMII to capture internal details of biological specimens in the self-driven mode (Fig. 4d). In contrast, conventional visible-light imaging only reveals the rough outlines of the samples without resolving their complex internal structures. Infrared imaging with the PMII, however, clearly captures fine internal features such as the antenna, occipital foramen, ocellus, and compound eye. Moreover, the PMII demonstrates broadband infrared imaging capability (Supplementary Fig. 21) and dynamic real-time infrared visualization (Supplementary Movies 4 and 5).

Discussion

In summary, we present a PMII that enables a resolution of 5799 ppi and a frame rate of 18.5 kHz for near-infrared (780-900 nm) visualization without relying on external power sources. Compared with commercial FPA devices and state-of-the-art upconversion devices, the PMII exhibits significant advantages in imaging resolution, frame rate, and power consumption. The stacked LSUs generate a sufficiently high photovoltage to independently drive the LEU, effectively converting near-infrared signals into visible emission. The monolithically integrated architecture of the PMII provides intrinsic flexibility, large-area scalability, and full compatibility

with room-temperature operation. Under near-infrared illumination, the device achieves a luminance of 47.2 cd m^{-2}, an *L*-LDR of 33 dB, and an $\eta_{p\text{-}p}$ of 0.116%, all without requiring external electrical bias. Moreover, the weak-light imaging threshold of ~80 μW cm^{-2} exceeds that of commercial infrared visualization cards. Compared with direct visible-light imaging, the PMII demonstrates clear advantages in biological imaging applications. This work establishes the PMII as a simplified, energy-efficient solution for infrared visualization, overcoming the structural complexity of conventional imaging systems and paving the way for advanced imaging technologies.

Methods

Material preparation

Zinc acetate dihydrate, ethanolamine, 2-methoxyethanol, chloroform, ZnO nanoparticle dispersion, and polyethylenimine ethoxylated (PEIE, 37 wt.% in H_2O) were obtained from Sigma-Aldrich. The acceptor material L8-BO was acquired from Solarmer Materials Inc, while MoO_3, TAPC, CBP, $Ir(ppy)_2(acac)$, B_3PyMPM, LiF and the donor material D18-Cl were purchased from Lumtec Corp. ITO-coated glass substrates and PET substrates were procured from South China Science & Technology Co., Ltd., and metals such as silver (Ag) and aluminum (Al) were supplied by Zhongnuo Advanced Materials Inc. The ZnO precursor solution was prepared by dissolving 110 mg of zinc acetate dihydrate, 31 μL of ethanolamine, and 1 mL of 2-methoxyethanol. This mixture was stirred overnight in air and subsequently filtered through a 0.45 μm PTFE filter. For the CGL, 7 mg of D18-Cl and 8.4 mg of L8-BO were dissolved in 1 mL of chloroform and stirred overnight in a glove box. The PEIE solution was diluted to 0.4 wt.% with 2-methoxyethanol and also filtered through a 0.45 μm PTFE filter before use. All materials were used as received without any further purification.

Device fabrication

Pre-patterned ITO substrates were initially cleaned with detergent, followed by sequential ultrasonication in deionized water, ethanol, acetone, and ethanol for 20 min each. After drying under a nitrogen flow, the substrates were treated with UV-ozone for 20 min. The ZnO precursor solution was spin-coated onto the ITO substrate at 5000 rpm for 30 s and annealed in air at 200 °C for 60 min. Subsequently, the CGL was deposited by spin-coating on the ZnO-coated substrate at

5000 rpm in a glove box for 40 s and annealed at 100°C for 10 min. For the ICL, the samples were transferred to a vacuum chamber and MoO_3 (10 nm) and Ag (1 nm) were deposited at a base vacuum pressure of 5×10^{-4} Pa. Afterwards, the samples were returned to the glove box. ZnO nanoparticle dispersion was spin-coated at 4000 rpm for 30 s and annealed at 100°C for 10 min. The PEIE layer was spin-coated at 4000 rpm for 30 s and similarly annealed at 100°C for 10 min. The CGL and ICL were repeatedly deposited on fabricated multi-layer stacked LSUs. Finally, TAPC (30 nm), CBP: 7%$Ir(ppy)_2(acac)$ (30 nm), B_3PyMPM (50 nm), LiF (1 nm), and Al (100 nm) were sequentially deposited through thermal evaporation. The active area of the PMII was defined by the overlapping region of the ITO anode and the Al cathode. For flexible devices, glass substrates were replaced with flexible PET substrates.

Device characterization

The absorption spectra were recorded using a UV-Vis-NIR spectrophotometer (Shimadzu UV-2600). The morphology of the films was characterized using transmission electron microscope (Hitachi TEM system) and atomic force microscopy (Asylum Research MFP-3D). The current-voltage-luminance characteristics of the PMII under varying light intensities were measured using a computer-controlled source measurement unit (Keithley 2450) with a luminance meter (PR 655, Photo Research) and the EL spectra were also recorded using a PR 655 spectrometer. All electrical and photoresponse characteristics of PMII were measured using a PDA analyzer. All biological samples were purchased from Xinxiang Hongye Edu. Instrument Co., Ltd., and Suzhou Shenying Optical Co., Ltd. The infrared viewing card (model TAC-A1) was purchased from KungShu Co., Ltd., and the standard resolution target used was USAF 1951, positive. All characterizations were conducted under ambient conditions. Unless otherwise specified, measurements were performed on rigid glass substrates under 830 nm near-infrared illumination. The resolution was determined based on the minimum resolvable line spacing (Supplementary Text 2)[24].

Data availability

Data supporting the findings of this study are available in the article and the ***Supplementary Information***. Any additional information can be obtained from the corresponding authors on reasonable request. Source Data are provided with this paper.

References

1. Vicentini, E., Wang, Z., Van Gasse, K., Hänsch, T. W. & Picqué, N. Dual-comb hyperspectral digital holography. *Nat. Photonics* **15**, 890-894 (2021).
2. Ji, A. *et al.* Quantitative phase contrast imaging with a nonlocal angle-selective metasurface. *Nat. Commun.* **13**, 7848 (2022).
3. Dorrah, A. H. *et al.* Light sheets for continuous-depth holography and three-dimensional volumetric displays. *Nat. Photonics* **17**, 427-434 (2023).
4. Hu, X. *et al.* Infrared-Light Visualization by Organic Upconversion Devices. *ACS Appl. Electron. Mater.* **5**, 5378-5385 (2023).
5. Li, N., Hu, X., Sui, X., Chen, Q. & Ng, T. N. Infrared Light Detection Technology Based on Organics. *ACS Appl. Electron. Mater.* **5**, 21-33 (2023).
6. Fu, C., Mu, G., Weng, K. & Tang, X. Advances in Organic Upconversion Devices. *Photonics* **11**, 808 (2024).
7. Xiao, J. *et al.* Optical Up-Conversion Devices Based on Organic and Inorganic Quantum Dots Materials. *J. Mater. Chem. C* **12**, 7833-7844 (2024).
8. Chen, J., Ban, D., Helander, M. G., Lu, Z. H. & Poole, P. Near-infrared inorganic/organic optical upconverter with an external power efficiency of >100%. *Adv. Mater.* **22**, 4900-4904 (2010).
9. Kim, D. Y., Song, D. W., Chopra, N., De Somer, P. & So, F. Organic Infrared Upconversion Device. *Adv. Mater.* **22**, 2260-2263 (2010).
10. Kim, D. Y. *et al.* PbSe nanocrystal-based infrared-to-visible up-conversion device. *Nano Lett.* **11**, 2109-2113 (2011).
11. Chen, J. *et al.* Hybrid organic/inorganic optical up-converter for pixel-less near-infrared imaging. *Adv. Mater.* **24**, 3138-3142 (2012).
12. Kim, D. Y., Lai, T. H., Lee, J. W., Manders, J. R. & So, F. Multi-spectral imaging with infrared sensitive organic light emitting diode. *Sci. Rep.* **4**, 5946 (2014).
13. Liu, S. W. *et al.* Transparent organic upconversion devices for near-infrared sensing. *Adv. Mater.* **27**, 1217-1222 (2015).
14. Gamal, A. E. & Eltoukhy, H. CMOS image sensors. *IEEE Circuits Devices Mag.* **21**, 6-20 (2005).
15. Lei, W., Antoszewski, J. & Faraone, L. Progress, challenges, and opportunities for HgCdTe infrared materials and detectors. *Appl. Phys. Rev.* **2**, 041303 (2015).
16. Zhang, Y. G. *et al.* Short-wave infrared InGaAs photodetectors and focal plane arrays. *Chin. Phys. B* **27**, 128102 (2018).
17. Mu, G. *et al.* Visible to mid-wave infrared PbS/HgTe colloidal quantum dot imagers. *Nat. Photonics* **18**, 1147–1154 (2024).
18. Steckel, J. S. *et al.* 1.62μm Global Shutter Quantum Dot Image Sensor Optimized for Near and Shortwave Infrared. *in Proc. IEEE Int. Electron Devices Meeting (IEDM)*, 23.24.21-23.24.24 (2021).
19. Alves, F. D. P. *et al.* NIR, MWIR and LWIR quantum well infrared photodetector using interband and intersubband transitions. *Infrared Phys. Technol.* **50**, 182-186 (2007).
20. Hu, P. *et al.* Vanadium Oxide: Phase Diagrams, Structures, Synthesis, and Applications. *Chem. Rev.* **123**, 4353-4415 (2023).
21. Stewart, J. W., Wilson, N. C. & Mikkelsen, M. H. Nanophotonic Engineering: A New Paradigm for Spectrally Sensitive Thermal Photodetectors. *ACS Photonics* **8**, 71-84 (2021).

22. Hsu, A. L. *et al.* Graphene-Based Thermopile for Thermal Imaging Applications. *Nano Lett.* **15**, 7211-7216 (2015).
23. Yu, H. *et al.* High-gain infrared-to-visible upconversion light-emitting phototransistors. *Nat. Photonics* **10**, 129-134 (2016).
24. Zhou, W. *et al.* Solution-processed upconversion photodetectors based on quantum dots. *Nat. Electron.* **3**, 251-258 (2020).
25. Dong, S. L. *et al.* Solution-Processed Efficient Organic Upconversion Device for Direct NIR Imaging. *Adv. Opt. Mater.* **12**, 2400912 (2024).
26. Du, X. Y. *et al.* Efficient Organic Upconversion Devices for Low Energy Consumption and High-Quality Noninvasive Imaging. *Adv. Mater.* **33**, 2102812 (2021).
27. Li, N., Eedugurala, N., Leem, D. S., Azoulay, J. D. & Ng, T. N. Organic Upconversion Imager with Dual Electronic and Optical Readouts for Shortwave Infrared Light Detection. *Adv. Funct. Mater.* **31**, 2100565 (2021).
28. Hany, R., Cremona, M. & Strassel, K. Recent advances with optical upconverters made from all-organic and hybrid materials. *Sci. Technol. Adv. Mater.* **20**, 497-510 (2019).
29. He, S. J., Wang, D. K., Yang, Z. X., Man, J. X. & Lu, Z. H. Integrated tandem device with photoactive layer for near-infrared to visible upconversion imaging. *Appl. Phys. Lett.* **112**, 243301 (2018).
30. Yang, D. *et al.* Near infrared to visible light organic up-conversion devices with photon-to-photon conversion efficiency approaching 30%. *Mater. Horiz.* **5**, 874-882 (2018).
31. Yu, B. H., Cheng, Y., Li, M., Tsang, S. W. & So, F. Sub-Band Gap Turn-On Near-Infrared-to-Visible Up-Conversion Device Enabled by an Organic-Inorganic Hybrid Perovskite Photovoltaic Absorber. *ACS Appl. Mater. Interfaces* **10**, 15920-15925 (2018).
32. Strassel, K. *et al.* Squaraine Dye for a Visibly Transparent All-Organic Optical Upconversion Device with Sensitivity at 1000 nm. *ACS Appl. Mater. Interfaces* **10**, 11063-11069 (2018).
33. He, Z. Y. *et al.* High-Quality Artery Monitoring and Pathology Imaging Achieved by High-Performance Synchronous Electrical and Optical Output of Near-Infrared Organic Photodetector. *Adv. Sci.* **10**, 2203870 (2023).
34. Shih, C. J. *et al.* Semi-Transparent, Pixel-Free Upconversion Goggles with Dual Audio-Visual Communication. *Adv. Sci.* **10**, 2302631 (2023).
35. Ding, H. *et al.* Microscale optoelectronic infrared-to-visible upconversion devices and their use as injectable light sources. *Proc. Natl. Acad. Sci. U.S.A.* **115**, 6632-6637 (2018).
36. Wei, Y. *et al.* Binary Organic Solar Cells Breaking 19% via Manipulating the Vertical Component Distribution. *Adv. Mater.* **34**, 2204718 (2022).
37. Zhu, C. *et al.* Vertical Phase Regulation with 1,3,5-Tribromobenzene Leads to 18.5% Efficiency Binary Organic Solar Cells. *Adv. Sci.* **10**, 2303150 (2023).
38. Yang, X. *et al.* High-Performance Up-Conversion Photodetectors with Zero-Barrier Interconnection via Self-Assembled Surface Dipoles. *Nano Lett.* **24**, 9385-9390 (2024).
39. Zhang, M. *et al.* Organic-Inorganic Hybrid Shortwave Infrared Up-conversion Imaging Devices with Ultra-high Refresh Rate and Excellent Resolution. *Adv. Mater. Technol.* **8**, 2300854 (2023).

Funding

W.H. discloses support for the research of this work from National Key Research and Development Program of China (grant number 2023YFB3611400) and National Natural Science

Foundation of China (grant number T2521003). J.W. discloses support for the research of this work from Guangdong Basic and Applied Basic Research Foundation (grant number 2024A1515010005) and Foundation of National Key Laboratory of Intense Pulsed Radiation Simulation and Effect (grant number NKLIPR2315). J.H. discloses support for the research of this work from National Natural Science Foundation of China (grant number 62305047).

Author contributions

X.H., J.W., L.G. and W.H. conceived the idea and designed the experiments. X.H. and L.G. fabricated the devices and conducted the characterization. J.W. and W.H. supervised the work. M.H. and C.H. performed the atomic force microscopy measurements. H.Y. and J.G. helped with discussions and data interpretation. X.H. wrote the original manuscript, and L.G. and S.D. finalized the manuscript. J.W., L.G., S.D., J.H. and W.H. reviewed and edited the paper. All authors discussed the results and commented on the paper.

Competing interests

The authors declare no conflict of interest.

Figures

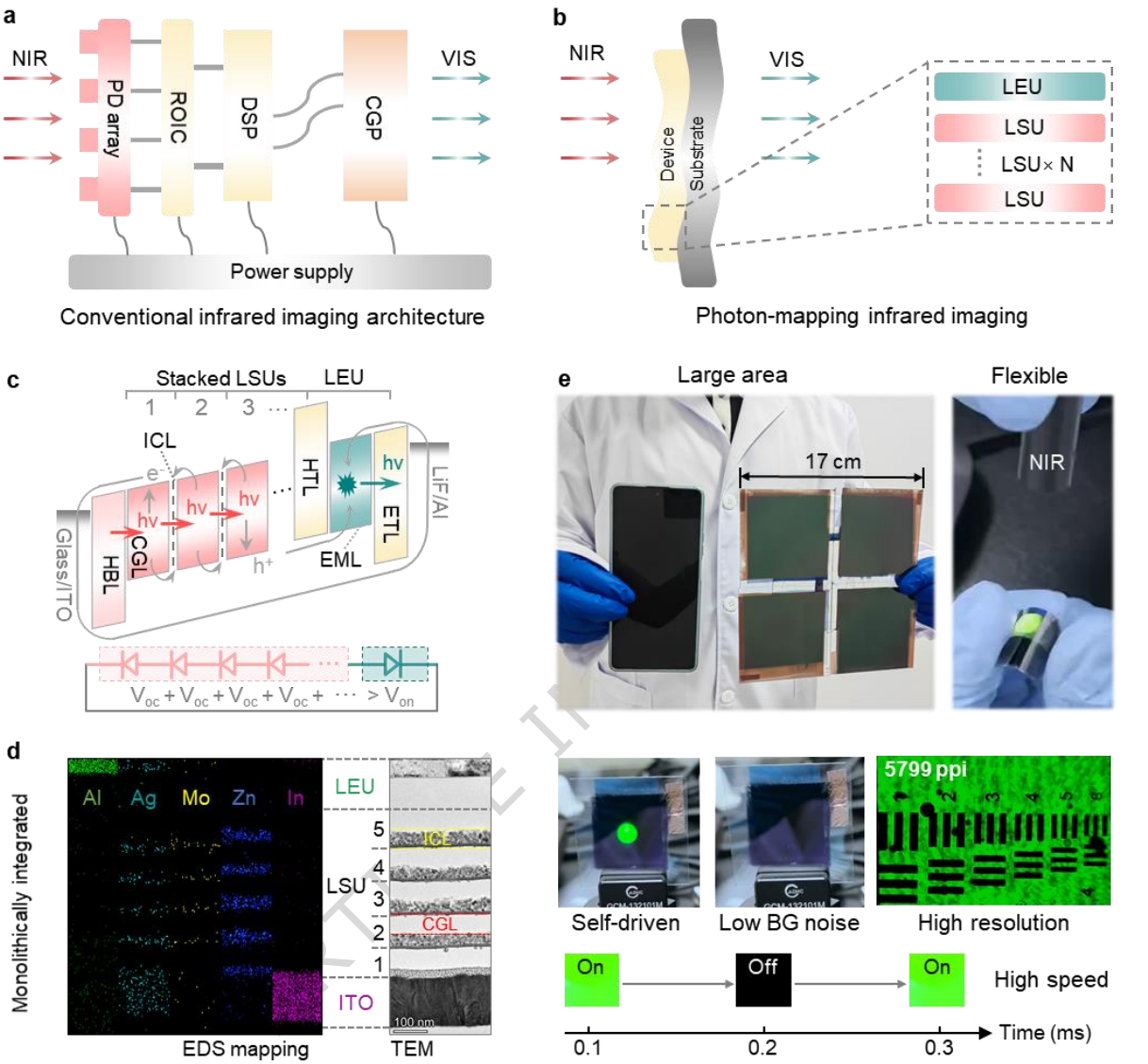

Figure 1. Monolithically integrated photon-mapping infrared imager (PMII). a Conventional infrared imaging architecture. PD: photodetector; ROIC: readout integrated circuit; DSP: digital signal processor; CGP: computer-vision graphics processor; VIS: visible; NIR: near infrared. **b** Monolithically integrated photon-mapping infrared imaging architecture. **c** Energy-level diagram illustrating that the photogenerated potential of the multi-stacked light-sensing units (LSUs) exceeds the turn-on voltage (V_{on}) of the light-emitting unit (LEU), which facilitates self-driven operation of the PMII. ICL: intermediate connection layer; CGL: charge generation layer; HTL: hole transport layer; HBL: hole blocking layer; EML: emission layer; ETL: electron transport layer; V_{oc}: open-circuit voltage. **d** Elemental distribution (Al, Ag, Mo, Zn, and In) obtained by energy-dispersive X-ray spectroscopy (EDS) mapping, aligned with a cross-sectional transmission electron microscopy (TEM) image of the PMII. **e** Optical photographs of the PMII, demonstrating its large-area, flexible, and self-driven characteristics, as well as its low background noise, high resolution, and high-speed performance.

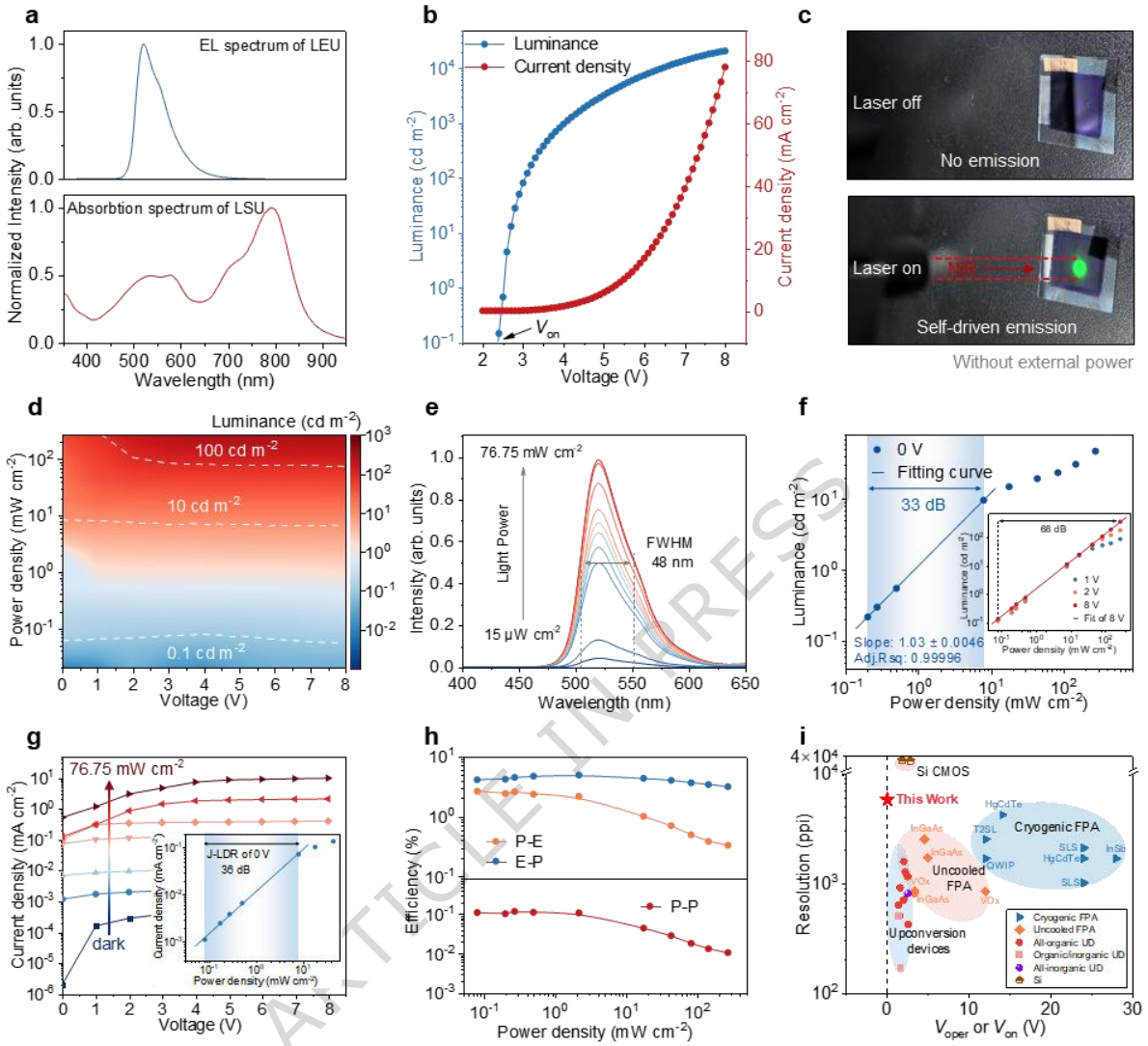

Figure 2. Performance evaluation of the PMII. a Normalized absorption spectrum of the LSU with a D18-Cl: L8-BO film as the charge generation layer, and the emission spectrum of the LEU with a CBP: 7%Ir(ppy)$_2$(acac) film as the emission layer (EL). **b** Current density-voltage-luminance curves of the LEU. **c** Photographs of the PMII without infrared illumination and under infrared illumination (8 mW cm^{-2}), in the self-driven mode. **d** 2D contour plot of luminance under various incident infrared power density and bias voltage. **e** Emission spectrum under different incident light power conditions in self-driven mode. **f** Self-driven luminance as a function of incident light power, with the inset showing the luminance linear dynamic range under varying bias voltages. **g** Current density-voltage characteristics under different incident light power conditions, with the inset showing the linear dynamic range of current density (*J*-LDR) in self-driven mode. **h** Variation of $\eta_{p\text{-}e}$, $\eta_{e\text{-}p}$ and $\eta_{p\text{-}p}$ with incident light power in self-driven mode. **i** Comparison of the PMII with the state-of-the-art infrared imaging techniques in terms of resolution and operating voltage (**Supplementary Tables 3 and 4**). FPA: focal plane array; CMOS: complementary metal-oxide-semiconductor.

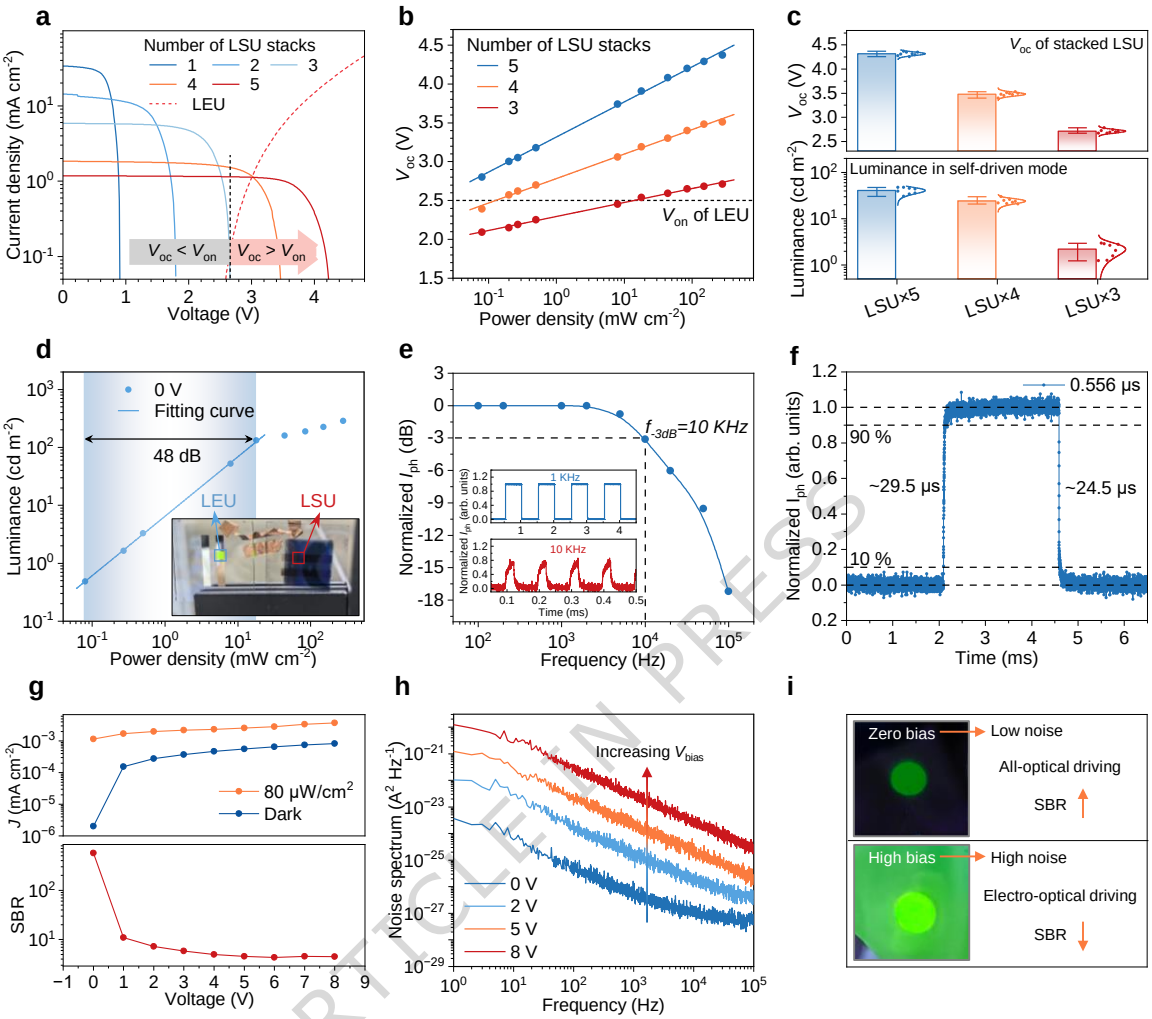

Figure 3. Stacking-dependent performance, dynamic response, and noise characteristics of the PMII. a Current density-voltage characteristics of LSUs with different stacking numbers measured at 85 mW cm^{-2} and the standalone LEU. **b** Variation of V_{oc} with incident light power for LSUs with different stacking layers. **c** Boxplots of V_{oc} for LSUs with different stacking layers and the corresponding luminance of PMII (statistical data obtained from more than eight devices). **d** Variation of luminance with incident light power for a device formed by directly connecting a five-layer stacked LSUs and a standalone LEU in series (inset shows the separated LSUs and LEU of the series-connected device). **e** Normalized photocurrent as a function of modulation frequency (inset shows the normalized photocurrent waveforms for 1 kHz and 10 kHz modulation). **f** Response time of the PMII. **g** Current density-voltage curves of the PMII in the dark and under 80 μW cm^{-2} illumination, and the corresponding signal-to-background ratio (SBR) versus bias voltage. **h** Noise spectra of the PMII under different bias voltages (V_{bias}). **i** Comparison of PMII operation under zero bias (self-driven mode) and high bias.

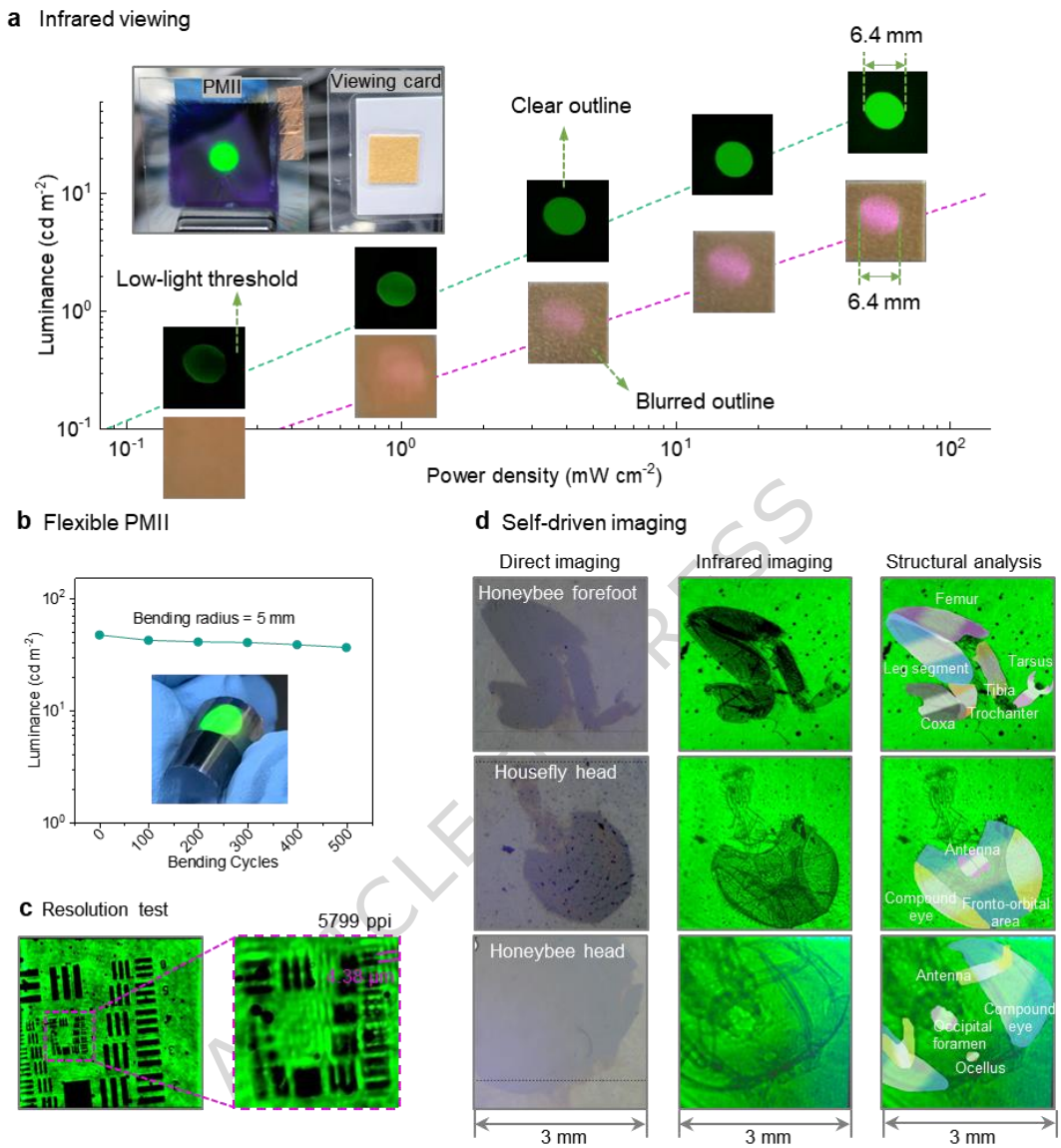

Figure 4. Application demonstration of the PMII. a Comparison of the actual light emission performance of the PMII and commercial infrared viewing card for a circular light spot laser under different incident power conditions. **b** Bending cycle measurement of the flexible PMII (830 nm, 20 mW cm^{-2} light illumination, and a bending radius of 5 mm). **c** The imaging resolution of the PMII was assessed in the self-driven mode using a resolution target. **d** Self-driven infrared imaging of various biological specimens using the PMII.

Editorial summary:

The study presents a self-powered, monolithically integrated infrared imager that converts invisible signals into visible light. Its flexible, lightweight design enables simple, large-area, high-quality imaging.

Peer review information: *Nature Communications* thanks the anonymous, reviewer(s) for their contribution to the peer review of this work. A peer review file is available.